Effects of Cu²⁺ doping and pressure on the exchange-mediated exciton dynamics in one-dimensional N(CH₃)₄MnCl₃

Lucie Nataf,[1,2] José Antonio Barreda-Argüeso,[1] Rafael Valiente,[3] Jesús González,[1] and Fernando Rodríguez[1,*]

[1]*MALTA Consolider Team, DCITIMAC, Facultad de Ciencias, Universidad de Cantabria, 39005 Santander, Spain*
[2]*Synchrotron SOLEIL, L'Orme des Merisiers, St. Aubin, Boîte Postale 48, 91192 Gif-sur-Yvette cedex, France*
[3]*MALTA Consolider Team, Departamento Física Aplicada, Universidad de Cantabria, 39005 Santander, Spain*

This work investigates the Mn²⁺ electronic structure and exciton dynamics in one-dimensional (1D) N(CH₃)₄MnCl₃ (TMMC) through time-resolved excitation/emission spectroscopy and absorption measurements in the 0–10 GPa pressure range for different Cu²⁺ doping concentrations. The local and crystal structures have been analyzed by Raman spectroscopy and x-ray absorption measurements at the Mn K edge showing that the 1D chain structure is maintained in the whole explored pressure range. We show that both the first Mn²⁺ absorption band, $^4T_1(G)$, and its associated emission band experience very large pressure redshifts, which are associated with the crystal anisotropy providing large axial ligand fields at the Mn²⁺ site that increase with pressure. The red emission at 633 nm shows a large pressure variation of 22 nm/GPa (50 meV/GPa) making TMMC a suitable probe for using as a photoluminescence (PL) pressure gauge in the low-pressure regime. The energy-transfer exciton dynamics and trapping at non-PL centers have been explained through changes of the intrachain Mn-Mn exchange interaction and Cu²⁺-trap concentration carried out by applying pressure and doping, respectively. The model demonstrates that an increase of exchange interaction favors both the pumping capability and energy transfer yielding exciton migration. Under these conditions, we show that pressure enhances the PL efficiency of TMMC provided that the Cu²⁺ concentration responsible for the PL quenching is below 0.001 mol %. However, between 0.001% and 0.1%, the PL intensity reduces with pressure, and above 0.1%, the PL is practically quenched even at ambient conditions.

I. INTRODUCTION

Most transition-metal (TM) halides and oxides do not exhibit photoluminescence (PL) at ambient conditions due to energy transfer between TM ions causing migration of the excitation and subsequent trapping at non-PL impurities or intrinsic defects, usually referred to as concentration quenching [1]. In concentrated TM compounds, the ground-state to excited-state transition mechanism and energy transfer between TM ions are mediated by the exchange-coupling interaction. Therefore an increase of the exchange interaction leads to increasing both the transition probability for exciton creation (Mn²⁺ excited state) and transfer probability. The knowledge of which process is the most sensitive to the exchange interaction determines whether an increase of the exchange interaction favors PL efficiency or trapping at non-PL centers. This elucidation requires a microscopic analysis of the different processes involved in the transition mechanisms and energy transfer, the analysis of which is fundamental for an eventual strategy in the design of highly efficient PL TM-concentrated compounds. Besides the exchange interaction, the energy-transfer probability depends on the overlap between the excitation and emission profiles and thus is temperature dependent. This overlap is minimum, or even zero, at low temperature and therefore energy transfer is severely reduced yielding highly efficient PL at low temperature as it is usually observed for most TM-concentrated compounds [1,2]. Thermal activation of the energy transfer ignites exciton migration and subsequent capture at non-PL traps. Interestingly, the probability of exciton trapping strongly depends on the crystal dimensionality and the presence of defects and impurities. For a given concentration of non-PL centers, $x = 1/N$, the number of steps (energy-transfer processes) for the exciton to reach a non-PL center is proportional to $N^{1/n}$, with $n = 1$, 2, or 3 being the crystal dimensionality. It implies that, independently of the energy-transfer process being as a random-walk or an exciton-driven motion, the time to reach a non-PL center decreases drastically on passing from 1D to two-dimensional (2D) and three-dimensional (3D) systems. It means that the probability of reaching an impurity by either process is the lowest in the 1D system and thus room-temperature PL in 1D TM-concentrated compounds is more likely.

These ideas explain why the N(CH₃)₄MnCl₃ (TMMC) crystal is a very efficient PL material at ambient conditions. In fact, TMMC has received considerable attention for structural, optical, and magnetic studies as an ideal 1D system [3–10]. Its crystal structure, shown in Fig. 1, consists of linear chains of face-sharing MnCl₆⁴⁻ octahedra of D_{3d} symmetry, linked by (CH₃)₄N⁺ cations through ionic interactions and hydrogen bonds [3,10]. This characteristic makes it suitable as an ideal 1D system of exchange-coupled Mn²⁺ ions since the intrachain Mn-Mn interaction is an order of magnitude larger than the interchain Mn-Mn interaction [10]. Hence, those properties related to the Mn-Mn exchange coupling, such as 1D magnetism [5,10] or 1D excitation transfer (migration) yielding PL [6–10], were intensively investigated on this model material. In contrast to 2D and 3D Mn²⁺ systems, the Mn²⁺ atomic arrangement in TMMC provides a 1D exciton confinement leading to substantial reduction of exciton capture by non-PL traps. In this way, it must be noted that the presence of non-PL exciton traps is eventually responsible for the absence of PL at

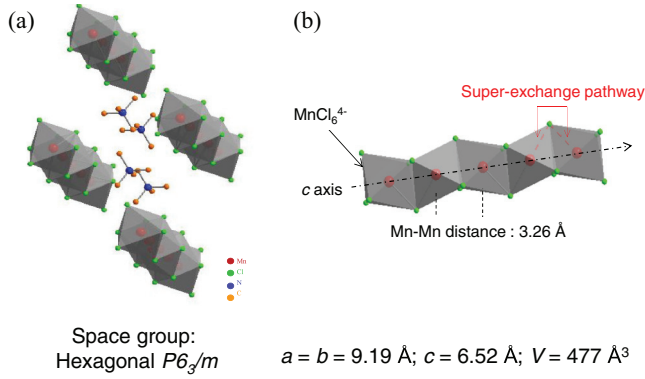*Corresponding author: fernando.rodriguez@unican.es

Space group:
Hexagonal $P6_3/m$

$a = b = 9.19$ Å; $c = 6.52$ Å; $V = 477$ Å^3

FIG. 1. (Color online) (a) Crystal structure of TMMC, showing the organic $(CH_3)_4N^+$ ions and the inorganic linear chains. H atoms have been omitted in the drawing for the sake of clarity. (b) Linear chain of face-sharing sixfold coordinated Mn^{2+} (D_{3d}).

ambient conditions in concentrated Mn^{2+} systems having 2D or 3D arrangements. So, BaMnF$_4$ [11] and Rb$_2$MnCl$_4$ [12] as 2D, and RbMnF$_3$ [13], MnF$_2$ [2], MnCl$_2$, and NH$_4$MnCl$_3$ [14] as 3D are illustrative examples of this behavior. Although all these compounds exhibit an intense PL at low temperature, it reduces upon increasing temperature and completely quenches at room temperature due to exciton migration and subsequent trapping by non-PL impurities. TMMC is an exception to this behavior. In general, those systems exhibiting exciton confinement due to low dimensionality or low exciton trapping by impurities are proper candidates to show room-temperature PL or to suppress it by intentional doping such as is illustrated in Fig. 2.

A recent correlation study between structural and magnetic properties in TMMC under high-pressure conditions [10] reveals that crystal compression is anisotropic, the MnCl$_6$ center increasing its axial distortion along the chain (hexagonal c axis) with pressure. This structural variation can favor an increase of the crystal field, Δ, and the splitting of the $^4T_1$ emitting state making it able to exhibit large PL pressure shifts.

Herein we investigate the PL properties of TMMC under high-pressure conditions aiming to explore how the intrachain Mn-Mn exchange interaction, J, and the crystal structure influence both PL intensity and associated pressure shifts. In particular, we are interested in elucidating whether increase of J improves the PL efficiency and whether pressure enhances the PL shift in TMMC so that it can be used as a precise pressure gauge in the middle- and low-pressure ranges, the latter being of great interest in bioscience and biotechnology. Owing to this, it must be pointed out that according to the material safety data sheets of the chemicals employed to synthesize TMMC, this material is poisonous. Therefore, TMMC must be handled with caution, particularly in biological environments. A method for embedding TMMC in biocompatible capsules is currently under progress.

II. EXPERIMENT

TMMC crystals were grown by slow evaporation from acidic aqueous solutions ($pH \approx 2$) containing 1:1 stoichiometric amounts of MnCl$_2$·4H$_2$O and N(CH$_3$)$_4$Cl. Intentional doping with Cu^{2+} was accomplished by mixing stoichiometric amounts of MnCl$_2$·4H$_2$O and CuCl$_2$·4H$_2$O (less than 1 mol %). The actual Cu^{2+} concentration from 0 (nominally pure) to 0.2 mol % was determined by atomic absorption spectroscopy. Their hexagonal crystal structure ($P6_3/m$ space group) was checked by x-ray diffraction using a Bruker D8 Advance diffractometer. Raman spectroscopy for experiments under pressure was performed with a triple monochromator Horiba-Jobin-Yvon T64000 spectrometer in subtractive mode backscattering configuration. It is equipped with liquid-nitrogen cooled charge-coupled device (CCD) detector. The 647-nm line of an Ar$^+$-Kr$^+$ laser was focused on the sample with a 20× objective for micro-Raman spectroscopy, keeping the laser power below 4 mW in order to avoid heating effects. Time-resolved excitation and emission spectra were obtained using the short pulses (8 ns) of the tunable Vibrant B 355 II
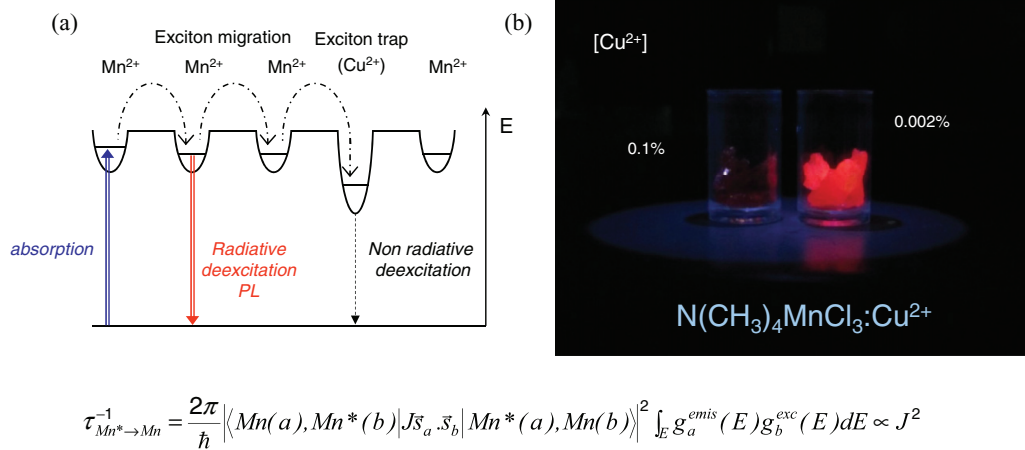

$$\tau^{-1}_{Mn^* \to Mn} = \frac{2\pi}{\hbar} \left| \left\langle Mn(a), Mn^*(b) \middle| J\vec{s}_a \cdot \vec{s}_b \middle| Mn^*(a), Mn(b) \right\rangle \right|^2 \int_E g_a^{emis}(E) g_b^{exc}(E) dE \propto J^2$$

FIG. 2. (Color online) (a) Schematic diagram of the Mn-Mn energy transfer (migration) and exciton capture by non-PL traps (Cu^{2+}) in 1D systems. (b) Effect of Cu^{2+} doping in the 370-nm-excited PL in TMMC. Note that for [Cu^{2+}] = 0.1 mol % PL is quenched at ambient conditions. The energy-transfer probability between one excited Mn^{2+}, $Mn^*(a)$, and one Mn^{2+} neighbor in the ground state, $Mn(b)$, is expressed by means of Fermi's golden rule. The effective density of final states is given by the overlap integral of the emission and excitation band profiles, defined as $\int g_a^{emis}(E)dE = \int g_b^{exc}(E)dE = 1$.

optical parametric oscillator (OPO) laser (Opotek Inc.). The excitation light was focused backwards on the sample with a 10-cm focal-length lens, and the PL light was collected upwards with an optical fiber attached to a $20\times$ microscope objective, and dispersed by a 0.32-m focal-length monochromator (Jobin-Yvon Triax 320). Time-resolved detection was carried out with an attached Horiba-Jobin-Yvon fast intensified CCD (i-CCD) detector. The excitation and emission spectra were corrected from the pulsed energy and the detection system, respectively. The time-resolved emission spectra were obtained upon excitation between 440 and 480 nm in the $^4T_2$ band of Mn^{2+} in TMMC in the 0–10 GPa range. The photon counting was for 1.5 ms after the excitation pulse. The average counting was 50 pulses for each excitation point. The time-resolved excitation spectra have been obtained by detecting the emission at the maximum wavelength using the same photon counting parameters employed for the emission spectra. Luminescence time-dependence measurements were done with an OPO laser tuned at the $^4T_2$ excitation maximum (440–480 nm) and photoluminescence, $I_{\mathrm{PL}}(t)$, was detected at the $^4T_1 \rightarrow {}^6A_1$ emission band maximum (630–800 nm) with the i-CCD using a variable delay time after pulse excitation from $t = 0$ to 5 ms in steps of 5 μs with a gate of 100 ms. The electronic absorption spectra as a function of pressure were performed using an improved microspectrophotometer specially adapted for using with diamond anvil cells (DACs). Hydrostatic pressure experiments in the 0–10 GPa range were carried out in a membrane DAC using silicone oil (Dow Corning 200 fluid 300 000 cSt) as pressure transmitting medium and with ruby PL as pressure calibrator. The absorption spectra were obtained using an oriented single crystal plate ($90 \times 100 \times 30 \ \mu$m^3) perpendicular to c.

III. RESULTS AND DISCUSSION

Figure 3 shows the room-temperature time-resolved emission and corresponding excitation spectra of TMMC in the 0–10 GPa range. The excitation spectra associated with the intense red emission at 633 nm (1.96 eV) show three bands characteristic of Mn^{2+} in nearly O_h symmetry (actually D_{3d} symmetry) peaking at 532 nm (2.33 eV), 444 nm (2.79 eV), and 420 nm (2.95 eV) at ambient conditions [15]. The bands observed in the excitation spectrum coincide with those measured in the absorption spectrum, but two additional bands related to higher-energy Mn^{2+} crystal-field transitions ($^6A_1 \rightarrow {}^4T_2(D)$ and $^4E(D)$) are also detected (Fig. 4). The first three bands observed in the excitation/absorption spectra are assigned within O_h symmetry to the Mn^{2+} crystal-field transitions: $^6A_1 \rightarrow {}^4T_1(G)$, $^4T_2(G)$, $^4A_1\,^4E(G)$, respectively. The emission peak at 633 nm (1.96 eV) takes place from the lowest-energy excited state and corresponds to the $^4T_1(G) \rightarrow {}^6A_1$ transition. Indeed the PL originates mainly from the lowest-energy excited state of the $^4T_1$ manifold, which is split by the axial field of the chain into $^4A_2 + {}^4E$ as shown in Fig. 5. The axial field is responsible for the additional redshift of the emission band, being displaced to larger wavelengths in comparison to the emission band of perfect octahedral MnCl$_6^{4-}$ centers [14,16]. In fact, the $^4T_1 \leftrightarrow {}^6A_1$ Stokes shift is about 0.2 eV along the AMCl$_3$:Mn^{2+} perovskite series [16] while it is 0.4 eV in TMMC (Fig. 5).

A. Pressure-induced shifts

The large pressure redshift exhibited by the excitation bands and particularly the emission band on passing from
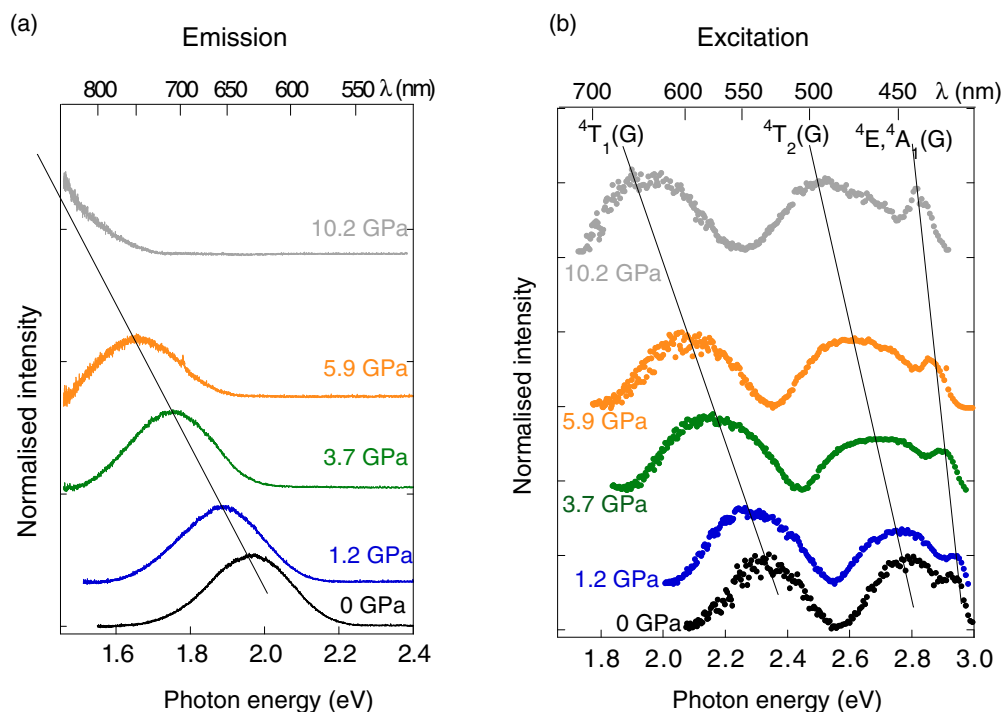

(a) Emission

(b) Excitation

FIG. 3. (Color online) (a) Pressure dependence of the room-temperature emission and (b) the corresponding excitation spectra of TMMC. Straight lines are guides for the eye. Numerical data are given in Fig. 5.
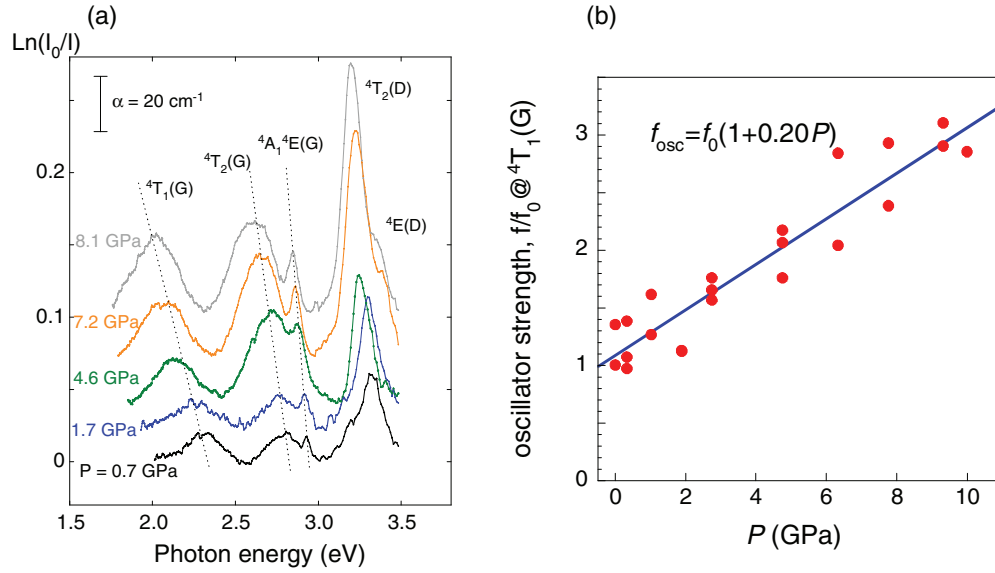
FIG. 4. (Color online) (a) Pressure dependences of the TMMC absorption spectrum and (b) $^4T_1(G)$ oscillator strength derived from the absorption band area. Data are normalized to sample volume through the TMMC equation of state [10].

ambient pressure to 10 GPa at room temperature (Figs. 3–5) is noteworthy. The three excitation bands $^4T_1$, $^4T_2$, and $^4A_1{}^4E$ peaking at 532 nm (2.33 eV), 444 nm (2.79 eV), and 420 nm (2.95 eV) at ambient pressure, respectively, shift to 626 nm (1.98 eV), 484 nm (2.56 eV), and 438 nm (2.83 eV) at 10 GPa. Note that the larger redshifts correspond to the strongly crystal-field-dependent $^4T_1$ and $^4T_2$ bands ($\Delta\lambda = 94$ and 40 nm, respectively, from 0 to 10 GPa), whereas it is smaller for the crystal-field-independent $^4A_1,{}^4E$ bands ($\Delta\lambda = 18$ nm) following the trend of the Tanabe-Sugano diagram (Fig. 6) upon increasing pressure; i.e., the Δ/B ratio [17]. The observed $^4A_1,{}^4E$ redshift must be ascribed to reduction of the Racah parameters B and C with pressure, while the larger redshifts of $^4T_1$ and $^4T_2$ are produced by additional contributions from the octahedral crystal field, Δ, which increases with pressure. Interestingly, the redshift undergone by the PL band is much

larger than the excitation redshifts. The emission band peaking at 633 nm (1.96 eV) at ambient conditions shifts to 855 nm (1.45 eV) at 10 GPa. It implies variations of $\Delta\lambda = 222$ nm ($\Delta E = 0.5$ eV) in this pressure range. The enormous PL redshift is even larger than the corresponding redshift of the first $^4T_1$ excitation band ($\Delta\lambda = 94$ nm) in the same pressure range, leading to an enormous increase of the Stokes shift, E_{SS} (Fig. 5). In fact, such an increase is contrary to the Stokes shift decrease observed in O_h-symmetry MnCl$_6^{4-}$ (Refs. [14,16]) and thus stresses the relevance of axial fields on the PL redshift. The $^4T_1$ and $^4T_2$ peak broadening with increasing pressure observed in the excitation/absorption spectra of Figs. 3 and 4 supports this view. In TMMC, the axial field along the chain (c direction) acting on Mn^{2+}(D_{3d}) increases the PL Stokes shift with respect to the octahedral Mn^{2+}(O_h) as indicated in Fig. 6. This unusually large PL redshift with pressure foresees 1D
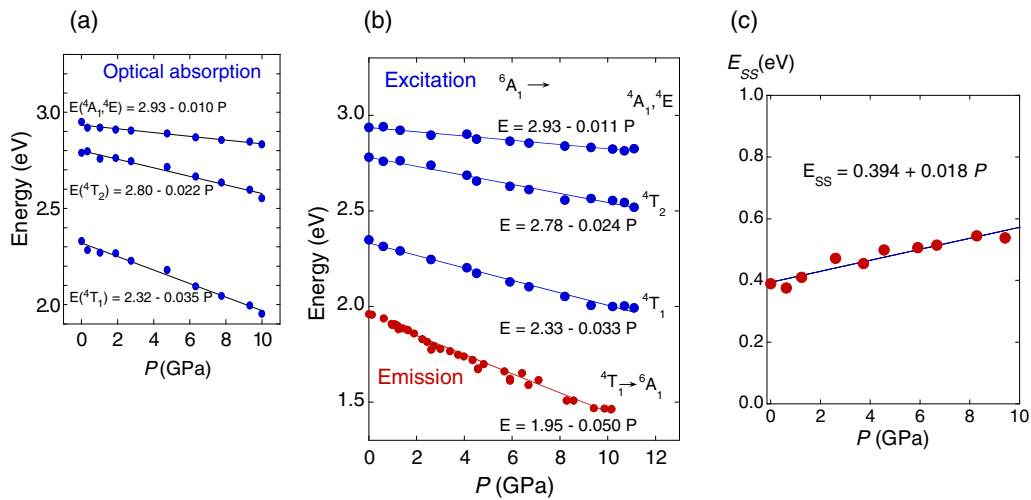

FIG. 5. (Color online) (a) Pressure dependence of Mn^{2+} crystal-field transition energies in TMMC obtained from (a) optical absorption, and (b) excitation and emission spectra. (c) Variation of the Stokes shift ($E_{ss} = E_{exc} - E_{emis}$) with pressure. Lines correspond to the least-squares linear fits to experimental data. Fitting equations $E(P)$ are indicated for each electronic transition.
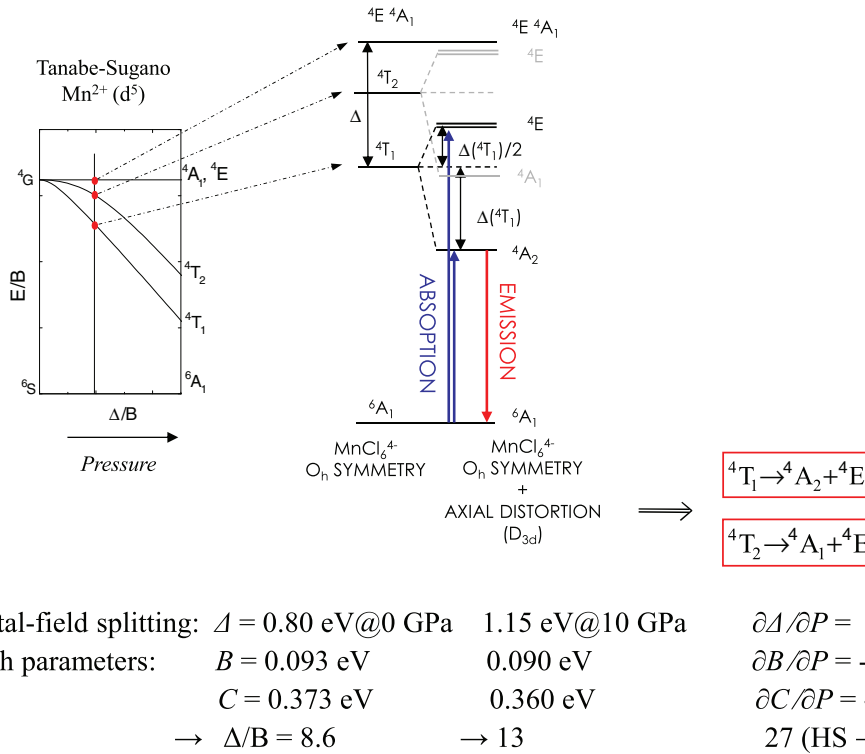
Crystal-field splitting:	Δ = 0.80 eV@0 GPa	1.15 eV@10 GPa	$\partial\Delta/\partial P$ = 35 meV/GPa
Racah parameters:	B = 0.093 eV	0.090 eV	$\partial B/\partial P$ = -0.3 meV/GPa
	C = 0.373 eV	0.360 eV	$\partial C/\partial P$ = -1.3 meV/GPa
	$\rightarrow$ Δ/B = 8.6	$\rightarrow$ 13	27 (HS $\rightarrow$ LS)

FIG. 6. (Color online) Simplified Tanabe-Sugano diagram for Mn²⁺ showing the effect of pressure on Δ/B. Black and red dots represent the experimental data for TMMC at ambient conditions and 10 GPa, respectively. The diagram shows the additional splitting of the $^4T_1(G)$, $^4T_2(G)$ states due to the axial crystal field along the chain. The emission mainly takes place from the low-energy $^4T_1$-split $^4A_2$ state and the excitation/absorption takes place from $^6A_1$ to $^4T_1-(^4A_2 + {}^4E)$. Parameters Δ, B, C, Δ/B, and their pressure derivatives were obtained by fitting the Mn²⁺ transition energies to the theoretical crystal-field energies [16,17].

systems of Mn²⁺ such as TMMC as potential PL sensors in the low-pressure regime. It was shown that TMMC (22.2 nm/GPa) [18] has similar capabilities as ruby (0.36 nm/GPa) [19] as a pressure gauge but in a pressure range 60 times smaller, let us say for P<2 GPa. This range is of great interest in bioscience and biotechnology as well as food science where the lack of suitable PL pressure sensors makes TMMC an ideal pressure gauge in this area, provided that it is encapsulated in biocompatible pressure transmitting material.

Figure 6 collects the spectroscopic parameters B, C, and Δ derived from the experimental transition energies taken from the excitation/absorption spectra, and their pressure rates. It must be noted that the volume dependence of Δ is quite weak in comparison with observation for many TM ions [20,21] exhibiting variations as $\Delta = \Delta_0(V_0/V)^{5/3}$, where Δ_0 and V_0 refer to the crystal-field splitting and crystal volume at ambient conditions, respectively. A recent review on the pressure dependence of the crystal field in TM systems is given elsewhere [22]. Taking into account that the bulk modulus and its pressure derivative for TMMC is B_0 = 10.9 GPa and B' = 10 (Ref. [10]), the exponent of the variation $\Delta(V)$ is 0.5, three times smaller than expected. However, this variation can be reconciled with a 5/3 exponent if we compare the variation of Δ with the local Mn-Cl distance, R. The $R(P)$ variation measured in the 0–1.7 GPa range by x-ray diffraction gives $R(P) = 2.57 - 0.020 \, P$ (in Å and GPa, respectively). It implies an R dependence of Δ as $\Delta = \Delta_0(R_0/R)$ [5,6], whose exponent is closer to 5 in line with variations found

for TM coordination compounds. This result points out that in organic/inorganic hybrid compounds such as TMMC the Mn²⁺ crystal-field analysis should be realized in terms of local volume (local distances) rather than crystal volume since the local volume of the stiff-bonded TM complex is decoupled from the crystal volume. The volume variation of the former is mainly imposed by covalent or ionic bonds while the crystal-volume variation is mainly governed by weaker hydrogen or van der Waals intermolecular bonding. Although the available diffraction data as a function of pressure are up to 1.7 GPa [10], the 1D chain structure of TMMC has been checked by Raman spectroscopy up to 7 GPa (Fig. S1 and Table S1 in the Supplemental Material, Refs. [23–26]) and x-ray absorption spectroscopy (Fig. S2, Refs. [23–26]).

B. Transition mechanism and energy transfer

The intrachain exchange-coupled Mn²⁺ ions in TMMC absorb light more efficiently than the isolated Mn²⁺ due to the exchange-induced transition mechanism [4,6,7,15]. The double-spin and parity-forbidden $^6A_1 \rightarrow {}^4\Gamma_i$ transitions (Γ_i = $^4T_1$, $^4T_2$, $^4A_1$ ^4E) are relaxed by the spin-orbit interaction and electron-phonon coupling to odd-parity modes, respectively. These interactions slightly activate the crystal-field transitions in centrosymmetric MnCl₆⁴⁻ yielding temperature-dependent oscillator strength of $f \approx 10^{-7}$ and associated PL lifetimes of 20 ms (300 K) or 55 ms (15 K) at ambient pressure as measured in Mn²⁺-doped $A M$Cl₃ perovskites (A = K,

Cs; M = Mg, Ca, Sr) [27]. However, these values contrast with those obtained for TMMC by optical absorption and lifetime measurements at ambient conditions [15]: $f \approx 10^{-5}$; $\tau = 0.8$ ms. This increase in oscillator strength (lifetime decrease) exhibited by the centrosymmetric $MnCl_6^{4-}(D_{3d})$ in TMMC with respect to the single-ion $MnCl_6^{4-}(O_h)$ in Mn^{2+}-doped $AMCl_3$ perovskites must be ascribed to the exchange mechanism [15]. The variation of the TMMC absorption spectrum with pressure shown in Fig. 4 clearly confirms this mechanism. The pressure-induced absorption enhancement of all crystal-field peaks is due to the increase of the exchange interaction with pressure. The increase of J with P was already reported by Tancharakorn *et al.* [10] by means of magnetic measurements under pressure in TMMC. Here we show the dominance of the exchange mechanism in the absorption spectra through the increase of the transition oscillator strength with pressure, $f_{OSC}(P)$. Figure 4 depicts the variation of $f_{OSC}(P)$ for the first $^4T_1$ transition. We obtain a pressure variation as $f_{OSC}(P) = f_0(1 + 0.20P)$, with f_0 being the ambient pressure oscillator strength of $^4T_1$. Although f_{OSC} is expected to be proportional to J, it must be noted that in absorption the exchange interaction involves both the ground and excited states, at variance with magnetic measurements whose J values involve only the $^6A_1$ ground state of the Mn^{2+}-coupled ions. Nevertheless, in either case an increase of J leads to an increase of f_{OSC}. In fact, the relative increase of $f_{OSC}(P)$ in the 0–10 GPa range agrees fairly well with the relative variation of J from magnetic measurements: $J(P) = J_0(1 + 0.2P)$, with $J_0 = -6.86$ cm^{-1}, although in that case the pressure range was limited to 0–1.7 GPa [10].

C. Migration and exciton trapping

The knowledge of the variation of $f_{OSC}(P)$ for the $^6A_1 \rightarrow {}^4T_1$ transition is crucial for determining whether increase of pressure in TMMC favors PL enhancement or exciton trapping at non-PL traps (PL quenching). The answer to this question requires knowledge of the deexcitation dynamics as a function of pressure and the non-PL trap concentration ($x = [Cu^{2+}]$). For this purpose we have done PL time-dependence measurements, $I(t)$, as a function P and x.

Figure 7 shows the time evolution of the PL, $I(t)$, at ambient conditions of TMMC containing a Cu^{2+} concentration of $x = 2 \times 10^{-5}$ (0.002 mol %). Contrary to nominally pure TMMC ($x < 10^{-6}$) in which $I(t)$ follows a single-exponential behavior as $I(t) = I_0 \exp(-t/\tau)$ with $\tau = 780$ μs, the PL time dependence follows a non-single-exponential behavior, the shape of which depends on the exciton migration processes and trapping at non-PL centers [6–9]. However, a simpler way of modeling the exciton dynamics as a function of the PL-quenching impurities (x) and the exchange interaction (J) can be made on the basis of the average lifetime defined as $\tau = \frac{\int_0^\infty t I(t) dt}{\int_0^\infty I(t) dt}$. Suitable values of this parameter can be obtained from the experimental $I(t)$ decay curves avoiding the sometimes delicate analysis of the $I(t)$ shape, due to errors in obtaining suitable $I(t)$ measurements in the limit $t \gg \tau$. This effect is particularly important in experiments dealing with low emission intensity like those attained in weakly luminescent materials or in high-pressure experiments using DAC. With the
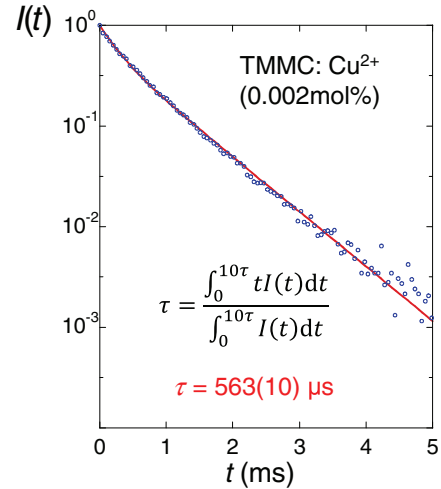

FIG. 7. (Color online) Semilog plot of the PL time dependence at 636 nm of TMMC doped with Cu^{2+} at ambient conditions. $I(t)$ was measured by detecting emission after pulsed excitation ($t = 0$) at 440 nm.

proposed procedure we overcome this problem by obtaining the main model parameters from precise $I(t)$ values. In fact, the sensitivity of the average lifetime is illustrated by its variation from $\tau = 780$ μs for pure TMMC ($x = 0$) to $\tau = 563$ μs for slightly Cu^{2+}-doped TMMC ($x = 2 \times 10^{-5}$) at ambient conditions.

The Mn^{2+} PL lifetime in 1D TMMC is related to the total deexcitation probability, τ^{-1}, which consists of two main contributions, namely, radiative probability, τ_{rad}^{-1}, and nonradiative probability, τ_{nr}^{-1}:

$$\tau^{-1} = \tau_{rad}^{-1} + \tau_{nr}^{-1}. \tag{1}$$

The radiative probability is associated with the $^4T_1 \rightarrow {}^6A_1$ crystal-field transition and involves the exchange mechanism and the vibronic activation, the sum of which is proportional to the transition oscillator strength:

$$\tau_{rad}^{-1}(P) = \tau_{exch}^{-1}(P) + \tau_{vib}^{-1}(P) \propto f_{OSC}(P). \tag{2}$$

Interestingly, the pressure dependence of this term is known experimentally through the absorption spectra as indicated in Fig. 4.

The nonradiative deexcitation probability relies on the exciton dynamics in the 1D Mn^{2+} chain. In particular, it basically depends on the time for exciton trapping at a non-PL center (Cu^{2+} in the present case). The average trapping time at Cu^{2+} depends on the concentration, x, and the intrachain energy-transfer probability between Mn^{2+} ions, $\tau_{Mn^* \rightarrow Mn}^{-1}$, through the expression

$$\tau_{nr}(P) = \frac{N_{steps}}{\tau_{Mn^* \rightarrow Mn}^{-1}}. \tag{3}$$

N_{steps} refers to the number of $Mn^* \rightarrow Mn$ energy-transfer processes required to reach a Cu^{2+} impurity. Given that there is a perfect matching between the Mn^{2+} emission spectrum and the Cu^{2+} absorption spectrum in 1D TMMC (Fig. S3, Refs. [23–26]) or the isomorphous Cd compound (TMCdC) [28], we assume that the transfer probability $Mn^* \rightarrow Cu$ is

much higher than the Mn*→Mn probability, and therefore a rapid transfer from Mn* to Cu is considered once the exciton reaches a Cu^{2+}-neighboring Mn^{2+} (Refs. [6–8]). Taking into account that the average number of Mn^{2+} between two Cu^{2+} impurities within the chain is just $1/x$, the average number of steps required for the excitation Mn* to reach a Cu^{2+} is $1/(4x)$ if the migration process is direct towards the impurity (exciton driven) or $1/(16x^2)$ if the migration is through a random-walk process. Therefore the nonradiative probability will depend on the type of migration process and can be written as

$$\tau_{nr}^{-1}(P) = 4x\tau_{Mn^*\to Mn}^{-1} \propto [Cu^{2+}]J^2 \qquad (4)$$

for a driven exciton or as

$$\tau_{nr}^{-1}(P) = 16x^2\tau_{Mn^*\to Mn}^{-1} \propto [Cu^{2+}]^2 J^2 \qquad (5)$$

for a random walk.

Following Fermi's "golden rule" (Fig. 2), it must be observed that the nonradiative probability is proportional to the square of the exchange interaction in both models, but depends linearly on x for a driven exciton and quadratically on x for a random-walk model. Thus, the x dependence of the lifetime can be the deciding factor in unveiling which process governs the exciton dynamics in TMMC.

At this stage it is important to know the role of exchange interaction on the PL intensity in TMMC. According to Eqs. (1)–(5), an increase of J increases τ_{rad}^{-1} and, consequently, the pumping capability and the radiative deexcitation probability, both yielding enhancement of PL intensity. On the other hand, τ_{nr}^{-1} also increases given that the energy-transfer probability $\tau_{Mn^*\to Mn}^{-1}$ increases and therefore the time for trapping at non-PL impurities decreases. The knowledge of which mechanism, τ_{rad}^{-1} or τ_{nr}^{-1}, is the dominant will determine the evolution of the PL efficiency with J or P.

Figure 8 shows the variation of the PL time dependence with pressure for a Cu^{2+}-doped sample with $x = 2 \times 10^{-5}$. It is worth noting that pressure reduces the PL lifetime.

The pressure effect on the PL lifetime for a given $[Cu^{2+}]$ is similar to an increase of $[Cu^{2+}]$ at ambient pressure (Fig. 9). However, their effect on the PL efficiency is quite different. Figure 8 also plots the measured PL lifetime as a function of pressure, and the calculated variation using Eq. (1) with $\tau_{rad}^{-1} = 1.3 \times 10^3(1 + 0.20P)$ and a Mn*→Mn transfer probability, given by $\tau_{Mn^*\to Mn}^{-1}(P) = \tau_{Mn^*\to Mn}^{-1}e^{0.27P}$ with $\tau_{Mn^*\to Mn}^{-1} = 2.5 \times 10^{10}$ s⁻¹ using a random-walk model, and 2.5×10^7 s⁻¹ by considering a driven-exciton model. This difference in the intrachain transfer probability is related to the different number of steps required to reach Cu^{2+} traps in each model. However, the latter Mn*→Mn probability is consistent with the exchange constant of TMMC, $J = 6.9$ cm⁻¹, measured by magnetic measurements. In fact, the probability, $J/h \approx 2 \times 10^{11}$ s⁻¹, agrees with the random-walk probability taking into account the reduction due to excitation and emission band overlap. The experimental variation $\tau(P)$ is well described with the proposed dynamics for exciton trapping.

Figure 9(a) shows the variation of the PL lifetime with $[Cu^{2+}]$, $\tau(x)$, at ambient conditions. In this situation, τ_{rad}^{-1}, $\tau_{Mn^*\to Mn}^{-1}$, and J do not depend on x, but τ_{nr}^{-1} does on x or x^2 depending on the exciton dynamics being driven exciton or random walk, respectively. It must also be noted that the $\tau(x)$ reduction with x is associated with the increase of τ_{nr}^{-1} by non-PL impurities and, consequently, it implies reduction of the PL efficiency due to a nonradiative deexcitation process by Cu^{2+}. Figure 9(b) plots the reciprocal PL lifetime, τ^{-1}, as a function of x together with the calculated variations $\tau^{-1}(x)$ for the two proposed models. The use of $\tau^{-1}(x)$ instead of $\tau(x)$ in the model analysis enhances the weighting of $\tau^{-1}(x)$ corresponding to higher Cu^{2+} concentrations. In fact, $\tau^{-1}(x)$ behaves linearly or quadratically with x, whereas a $\tau(x)$ plot is not sensitive enough to reveal x dependences as x or x^2 since τ rapidly decreases with x in both models. Although a simple inspection of Fig. 9(b) suggests that the exciton-driven model applies better than the random walk to describe the
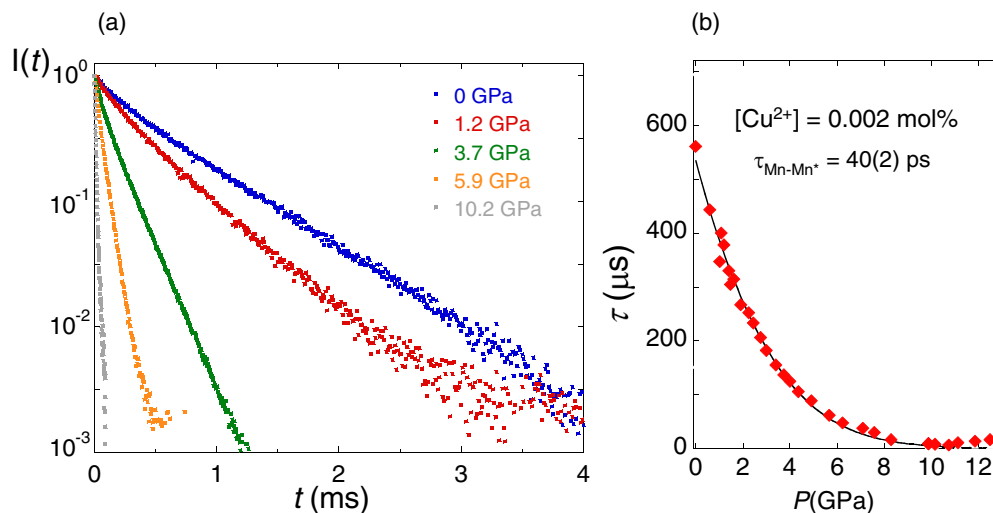

FIG. 8. (Color online) (a) Semilog plot of the PL time dependence, $I(t)$, between 636 nm (ambient pressure) and 800 nm ($P = 10$ GPa) of TMMC doped with 0.002 mol % Cu^{2+}, and (b) corresponding variation of τ with pressure. Line corresponds to best fit with Eqs. (1)–(5). The obtained intrachain Mn-Mn* hopping time and its pressure dependence is given by $\tau_{Mn^*\to Mn}^{-1}(P) = \tau_{Mn^*\to Mn}^{-1}e^{0.27P}$ with $\tau_{Mn^*\to Mn}^{-1}(P) = 2.5 \times 10^{10}$ s⁻¹, i.e., $\tau_{Mn^*\to Mn} = 4 \times 10^{-11}$ s.
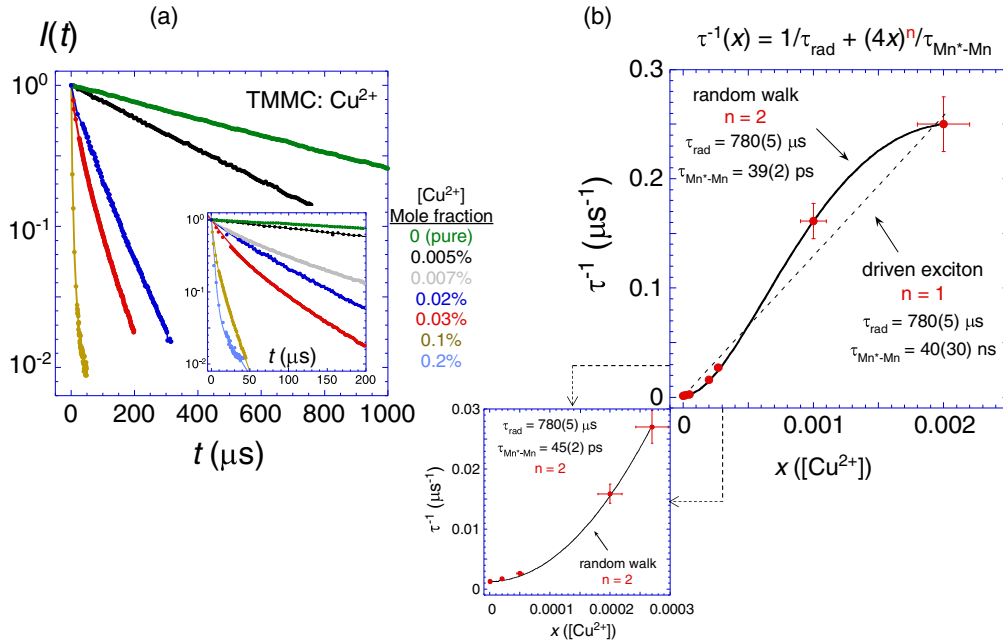
FIG. 9. (Color online) (a) Semilog plot of the PL time dependence, $I(t)$, at 636 nm of TMMC doped with Cu^{2+} as a function of x at ambient pressure. The inset shows a magnification of $I(t)$ in the 0–200 μs range. (b) Plot of $\tau^{-1}(x)$ vs x. Lines correspond to best fit with Eqs. (4) and (5) using the driven-exciton ($n = 1$) and random-walk ($n = 2$) models. A magnification of the $\tau^{-1}(x)$ plot in the low-doping-concentration range is shown bottom left. Note the quadratic dependence of $\tau^{-1}(x)$ with x for diluted samples ($x < 0.0003$) characteristic of random-walk exciton dynamics. Deviation from the quadratic behavior for $x > 0.0003$ is ascribed to Cu^{2+} aggregates (see text for explanation).

exciton dynamics in the whole Cu^{2+} concentration range as $\tau^{-1}(x) \propto x$ [dotted line in Fig. 9(b)], $\tau^{-1}(x)$ exhibits a perfect quadratic behavior for low Cu^{2+} concentrations ($x < 0.0003$), characteristic of a random-walk dynamics. For $x > 0.0003$, experimental $\tau^{-1}(x)$ data deviate considerably from a quadratic behavior if we assume that Cu^{2+} is homogeneously distributed in TMMC. However the intrachain transfer probability obtained through the exciton-driven model is not consistent with values obtained at low Cu^{2+} concentrations using a random-walk model. This complex behavior of $\tau^{-1}(x)$ for $x > 0.0003$ can be explained by a random walk if we consider Cu^{2+} aggregates with increasing x. Taking into account the solubility limit in TMMC is about $x \approx 0.002$, there must be

a significant fraction of Cu^{2+} aggregates as the concentration increases for $x > 0.0003$. The effective Cu^{2+} traps in TMMC can be described phenomenologically replacing x for $xe^{-x/\alpha}$. This expression accounts for the formation of aggregates in the simplest form using a unique effective parameter α representing a concentration limit of dilution for Cu^{2+}. We fairly account for $\tau^{-1}(x)$ in the whole x range by incorporating this correction in the random-walk model. Figure 9(b) shows the fitting result with $\alpha = 0.0021$. Thus $\tau^{-1}(x)$ clearly indicates that exciton dynamics in TMMC is governed by a random-walk model for all Cu^{2+} concentrations, but its deviation from a x^2 behavior is ascribed to aggregation processes and subsequent Cu^{2+} precipitation at higher concentration ($x > 0.002$). The
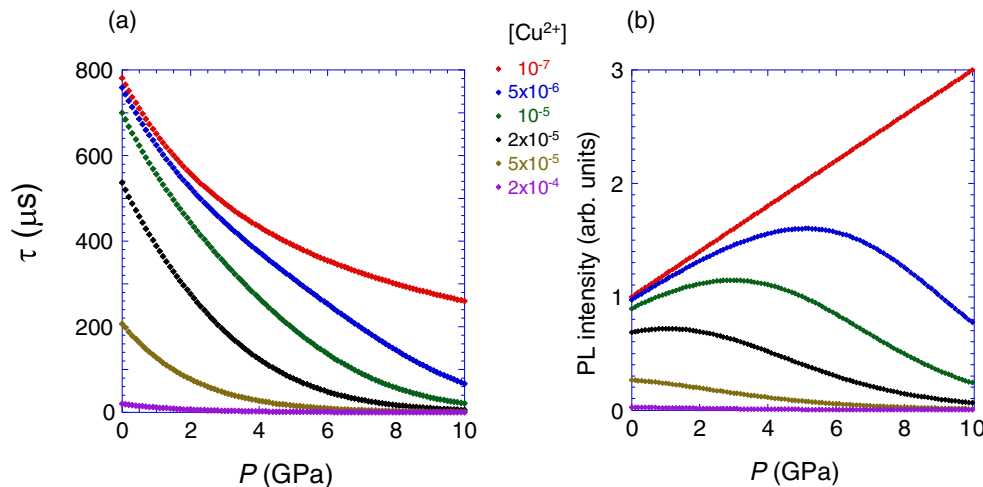

FIG. 10. (Color online) (a) Calculated τ and (b) PL intensity in TMMC doped with Cu^{2+} as a function of pressure for different Cu^{2+} concentrations through Eqs. (1)–(5).

fit energy-transfer time, $\tau_{\mathrm{Mn}^* \to \mathrm{Mn}} = 40$ ps, is consistent with the Mn-Mn superexchange constant measured by magnetic measurements in TMMC [10].

Interestingly, the PL lifetimes obtained as a function of P and x allow us to foresee the evolution of both $\tau(x, P)$ as well as the relative PL intensity, $I_{\mathrm{rel}}(x, P)$, through the luminescence quantum yield defined as $\eta(x, P) = \frac{\tau_{\mathrm{rad}}^{-1}}{\tau_{\mathrm{rad}}^{-1} + \tau_{\mathrm{nr}}^{-1}}$, where $\tau_{\mathrm{rad}}^{-1}(P) \propto f_{\mathrm{OSC}}(P)$. The relative-intensity parameter is then given by $I_{\mathrm{rel}}(x, P) = C_0 \times f_{\mathrm{OSC}}(P) \times \eta(x, P)$, where C_0 is constant, and provides the variation of PL intensity as a function of pressure or Cu^{2+} concentrations under the same pumping conditions at the band maximum. Figure 10 depicts the model calculations for different Cu^{2+} concentrations (x: 10^{-7}–10^{-4}) in the 0–10 GPa range.

A salient conclusion is the increase of PL intensity with pressure for $x < 10^{-5}$ (low impurity concentration). Although the decrease of PL lifetime with pressure is due to increase of the transition oscillator strength and energy-transfer probability, the former variation is dominant for low [Cu^{2+}] concentrations. Therefore the absorption enhancement increases the pumping capability augmenting the PL intensity. However, this is not the situation for $x > 10^{-5}$ since the increase of nonradiative probability with pressure due to both x and $\tau_{\mathrm{Mn}^* \to \mathrm{Mn}}$ yields reduction of PL intensity. The present results indicate that in 1D TMMC pressure enhances the PL efficiency of the material provided that the non-PL impurity concentration responsible for the PL quenching is below $x < 10^{-5}$. Between $x = 10^{-5}$ and $x = 10^{-3}$, the PL intensity decreases with x at ambient pressure and with pressure for any concentration. For $x > 10^{-3}$ the PL is practically quenched at ambient conditions as indicated Fig. 2(b).

IV. CONCLUSIONS

Here we show that both the crystal-field excitation and corresponding red emission bands of the 1D TMMC experience very-large-pressure redshifts, which are associated with the anisotropic crystal compressibility, providing large axial ligand fields at the Mn^{2+} site. The red emission shows the largest pressure rate of 22 nm/GPa (50 meV/GPa), 60 times larger than ruby, making TMMC a suitable compound for using as a pressure gauge in the low-pressure regime. The exciton dynamics and trapping at non-PL centers have been explained by an energy-transfer model completely governed by the Mn-Mn exchange interaction yielding a random-walk migration within the chain to non-PL centers (Cu^{2+}) as it was demonstrated through time-resolved spectroscopy as a function of the applied pressure and Cu^{2+} doping. The model foresees that increase of exchange interaction favors both the pumping capability and the energy-transfer probability. However, we show that pressure enhances the PL efficiency of TMMC provided that the Cu^{2+} concentration responsible for the PL quenching is below 0.001 mol %. Above 0.1 mol %, the PL is practically quenched at ambient conditions. A salient conclusion derived from lifetime data analysis concerns the aggregation of Cu^{2+} in TMMC even for low doping concentrations ($x > 0.0002$); the solubility limit is around 0.002. This conclusion is important since it enforces to reconsider previous exciton dynamical models developed on the assumption that Cu^{2+} is homogeneously diluted in TMMC for all concentrations below 0.1%.

[1] B. Henderson and G. F. Imbusch, *Optical Spectroscopy of Inorganic Solids* (Oxford University Press, New York, 1989).

[2] I. Hernández, F. Rodríguez, and H. D. Hochheimer, Phys. Rev. Lett. **99**, 027403 (2007).

[3] B. Morosin and E. J. Graeber, Acta Crystallogr. **23**, 766 (1967).

[4] P. Day and L. Dubicki, J. Chem. Soc., Faraday Trans. **69**, 363 (1973).

[5] R. E. Caputo and R. D. Willett, Phys. Rev. B **13**, 3956 (1976).

[6] R. A. Auerbach and G. L. McPherson, Phys. Rev. B **33**, 6815 (1986).

[7] R. Knochenmuss and H. U. Güdel, J. Chem. Phys. **86**, 1104 (1987).

[8] M. F. Herman, W. J. Rodríguez, and G. L. McPherson, Chem. Phys. Lett. **144**, 541 (1988).

[9] R. Kroon, H. Fleurent, and R. Sprik, Phys. Rev. E **47**, 2462 (1993).

[10] S. Tancharakorn, F. P. A. Fabbiani, D. R. Allan, K. V. Kamenev, and N. Robertson, J. Am. Chem. Soc. **128**, 9205 (2006).

[11] T. Tsuboi and W. Kleemann, Phys. Rev. B **27**, 3762 (1983).

[12] T. Tsuboi and K. Iio, Phys. Status Solidi B **179**, K47 (1993).

[13] F. R. Wunsch and W. Gebhardt, J. Phys. Condens. Matter **1**, 855 (1989).

[14] I. Hernández and F. Rodríguez, J. Phys.: Condens. Matter. **15**, 2183 (2003).

[15] Y. Rodríguez-Lazcano, L. Nataf, and F. Rodríguez, Phys. Rev. B **80**, 085115 (2009).

[16] M. C. Marco-de-Lucas, F. Rodríguez, H. U. Güdel, and N. Furer, J. Lumin. **60-61**, 581 (1994).

[17] S. Sugano, Y. Tanabe, and H. Kamimura, *Multiplets of Transition-Metal Ions*, (Academic Press, New York, 1970).

[18] L. Nataf, F. Rodríguez, R. Valiente, and J. González. High Pressure Res. **29**, 653 (2009).

[19] K. Syassen, High Pressure Res. **28**, 75 (2008).

[20] D. R. Stephens and H. G. Drickamer, J. Chem. Phys. **35**, 429 (1961).

[21] H. G. Drickamer and C. W. Frank, *Electronic Structure, Electronic Transitions and the High Pressure Chemistry and Physics of Solids* (Chapman and Hall, London, 1973).

[22] M. Grinberg, Opt. Mater. **28**, 26 (2006).

[23] See Supplemental Material at http://link.aps.org/supplemental/10.1103/PhysRevB.89.115120 for experimental details and technical procedures.

[24] F. Baudelet, Q. Kong, L. Nataf, J. D. Cafun, A. Congeduti, A. Monza, S. Chagnot, and J. P. Itie, High Press. Res. **31**, 136 (2011).

[25] P. S. Peercy, B. Morosin, and G. A. Samara, Phys. Rev. B **8**, 3378 (1973).

[26] M. N. Braudt, M. Couzi, N. B. Chanh, and A. Gomez-Cuevas, J. Phys.: Condens. Matter **2**, 8229 (1990).

[27] M. C. Marco-de-Lucas, F. Rodríguez, C. Prieto, M. Verdaguer, M. Moreno, and H. U. Güdel, Radiat. Eff. Defects Solids **135**, 1 (1995).

[28] R. Valiente, M. C. Marco-de-Lucas, and F. Rodríguez, J. Phys.: Condens. Matter **6**, 4527 (1994).